Chemical Science

ROYAL SOCIETY OF CHEMISTRY

EDGE ARTICLE

View Article Online
View Journal | View Issue

Cite this: *Chem. Sci.*, 2024, **15**, 2221

All publication charges for this article have been paid for by the Royal Society of Chemistry

Received 20th September 2023
Accepted 3rd January 2024

DOI: 10.1039/d3sc04947g

rsc.li/chemical-science

Xanthene-based near-infrared chromophores for high-contrast fluorescence and photoacoustic imaging of dipeptidyl peptidase 4†

Pei Lu, Si-Min Dai, Huihui Zhou, Fenglin Wang, * Wan-Rong Dong * and Jian-Hui Jiang

Near-infrared (NIR) chromophores with analyte tunable emission and absorption properties are highly desirable for developing activatable fluorescence and photoacoustic (PA) probes for bioimaging and disease diagnosis. Here we engineer a class of new chromophores by extending the π-conjugation system of a xanthene scaffold at position 7 with different electron withdrawing groups. It is demonstrated that these chromophores exhibit pH-dependent transition from a spirocyclic "closed" form to a xanthene "open" form with remarkable changes in spectral properties. We further develop fluorescence and PA probes by caging the NIR xanthene chromophores with a dipeptidyl peptidase 4 (DPPIV) substrate. *In vitro* and live cell studies show that these probes allow activatable fluorescence and PA detection and imaging of DPPIV activity with high sensitivity, high specificity and fast response. Moreover, these two probes allow high-contrast and highly specific imaging of DPPIV activity in a tumour-bearing mouse model *in vivo via* systemic administration. This study highlights the potential of a xanthene scaffold as a versatile platform for developing high-contrast fluorescence and PA molecular probes.

Introduction

Small molecule-based fluorescence and photoacoustic (PA) probes hold great promise for bioimaging and disease diagnosis. Activatable fluorescent probes responsive to cancer-associated biomarkers and treatment-relevant proteases have been developed for tumor imaging and anti-cancer assessment *in vivo*.[1–3] However, fluorescence imaging approaches generally possess a shallow penetration depth (<1 mm) and low spatial resolution due to tissue scattering and absorption.[4,5] PA imaging is emerging as a powerful imaging modality that utilizes optical signals as an excitation source and acoustic signals as the output, allowing imaging with deep tissue penetration depths (centimeter) and excellent spatial resolution (100 μm).[6,7] Activatable small-molecule PA probes have been developed to image cancer-associated enzymes and small molecules.[8,9] Nonetheless, the development of high-contrast fluorescence and PA imaging probes relies on the availability of chromophores with near-infrared (NIR) excitation/emission wavelengths, desirable quantum yields and analyte-tunable absorption or emission profiles.

Among the various chromophores, xanthene-based chromophores such as fluorescein, rhodamine and their hybrid (rhodol) have received great interest owing to their desirable photophysical properties.[10,11] Xanthene-based chromophores can exist in a spirocyclic "closed" form with a disrupted conjugation system and zwitterionic "open" form with large π-conjugation. More importantly, the spirocyclic form with short absorption and negligible emission can be switched to the zwitterionic form with a long absorption and emissive state by analytes, allowing the development of high-contrast fluorescence and PA imaging probes. To engineer xanthene based NIR chromophores, a typical approach is substituting the central oxygen atom with other elements such as Si, S and P, affording chromophores with pronounced bathochromic shifts and NIR emission.[12–14] These chromophores generally exhibited small Stokes shifts. An alternative approach is conjugating xanthene with varying π-conjugation systems at different positions.[15–20] For instance, π-conjugated expansion at position 3 afforded chromophores with NIR absorption wavelengths.[15,16] However, some of these chromophores always exist in a spirocyclic "closed" form or xanthene "open" form at physiological pH, preventing the design of analyte-activatable fluorescence/PA imaging probes.[17,18] Recently, a type of xanthene-based NIR-II chromophore has been engineered by π-conjugated expansion at positions 3 and 6.[19,20] However, they intended to exist in the spirocyclic form and the carboxylic moiety needs to be esterified to inhibit the lactonization. Thus, the development of new

State Key Laboratory of Chemo/Bio-Sensing and Chemometric, College of Chemistry and Chemical Engineering, Hunan University, Changsha, 410082, P. R. China. E-mail: fengliw@hnu.edu.cn; wanrongdong@hnu.edu.cn

† Electronic supplementary information (ESI) available. See DOI: https://doi.org/10.1039/d3sc04947g

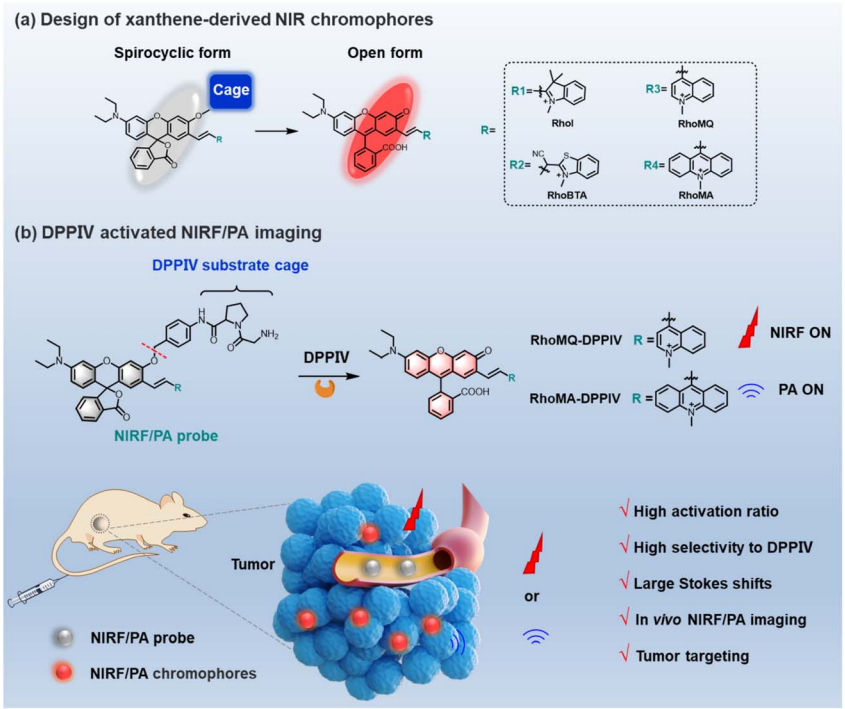

Scheme 1 (a) Schematic illustration for the design of xanthene-derived NIR chromophores with tunable spirocyclic "closed" and xanthene "open" properties. (b) Schematic illustration for the mechanism of probes RhoMQ-DPPIV and RhoMA-DPPIV for NIRF/PA imaging of DPPIV activity *in vivo*.

xanthene-based NIR chromophores that exhibit analyte-modulated photophysical properties is highly desirable.

Here we report a class of new xanthene-based chromophores which exhibit a transition from a spirocyclic "closed" form to a zwitterionic "open" form through decaging of the phenolic hydroxyl group, allowing the development of high-contrast fluorescence and PA imaging probes. We first engineer a series of new xanthene chromophores by conjugating rhodol with different electron withdrawing groups including indolium (RhoI), benzothiazolium acetonitrile (RhoBTA), methylquinoline (RhoMQ) and methylacridine (RhoMA) at position 7 (Scheme 1a). It is demonstrated that these chromophores are predominantly in the zwitterionic form at neutral pH and spirocyclic form at acidic pH (<5.2). This result suggests that π-conjugation expansion of rhodol at position 7 holds great promise for developing activatable molecular probes *via* caging the phenolic hydroxyl group. As a proof of demonstration, we choose RhoMQ and RhoMA to develop an NIR fluorescence and a PA probe for imaging dipeptidyl peptidase 4 (DPPIV) activity (Scheme 1b). DPPIV is a transmembrane glycoprotein with serine protease activity that can cleave N-terminal dipeptides from polypeptides with proline preferentially at the penultimate position.[21–24] It is recognized that DPPIV is abnormally expressed in various pathological processes such as diabetes and malignant tumours, and has become an important diagnostic biomarker and therapeutic target.[25,26] We design an NIR fluorescence probe (RhoMQ-DPPIV) and a PA probe (RhoMA-DPPIV) for DDPIV by caging the phenolic hydroxyl groups of RhoMQ and RhoMA with the enzyme recognition group (Gly–Pro) *via* a self-immolative *p*-aminobenzyl alcohol linker, respectively. We demonstrate that these probes exhibit high sensitivity, high specificity and high signal-to-background ratios toward DPPIV activity *in vitro* and *in vivo via* NIR fluorescence/PA imaging. To our knowledge, this is the first time that the activity of DPPIV is imaged *via* systemic administration *in vivo*. Our study highlights the potential of xanthene-based chromophores for developing high-contrast molecular probes for biological studies.

Results and discussion

Synthesis and characterization of NIR chromophores

To engineer xanthene-derived NIR chromophores that exhibited analyte-tunable spirocyclic and zwitterionic forms, we started to conjugate xanthene with different electron withdrawing groups at the 7 position (Scheme S1†). Briefly, a rhodol derivative with an aldehyde at the 7 position (Rho-A) was obtained by refluxing 3-diethylaminophenol and phthalic anhydride in methylbenzene, followed by reacting with 2,4-dihydroxybenzaldehyde in methanesulfonic acid. Then, Rho-A was conjugated with indolium, benzothiazolium acetonitrile, methylquinoline and methylacridine, respectively, to obtain RhoI, RhoBTA, RhoMQ and RhoMA *via* a Knoevenagel condensation reaction. The successful synthesis of RhoI, RhoBTA, RhoMQ and RhoMA was characterized by ^{1}H NMR, ^{13}C NMR and HR-ESI-MS, respectively.

With these four chromophores, we investigated their photophysical properties by absorption and fluorescence

spectroscopy. RhoI, RhoBTA, RhoMQ and RhoMA exhibited maximum absorption at 600, 536, 580 and 690 nm, respectively, in pH 7.4 buffer (Fig. 1a). These varied absorption peaks were presumably due to their different conjugation systems and donor–π–acceptor structures. The molar absorption coefficients for RhoI, RhoBTA, RhoMQ and RhoMA were calculated to be 3.08×10^5, 1.92×10^5, 1.99×10^5, and 0.27×10^5 M^{-1} cm^{-1}, respectively (Table S1†). Besides, all four conjugates exhibited varied absorption spectra in solvents of different polarity, which could be ascribed to their donor–π–acceptor structures and spirocyclic-forming switchability (Fig. S1†).[13,27] Fluorescence spectra showed that these chromophores were highly emissive with emission peaks at 727 nm ($\varphi = 0.088$), 575 nm ($\varphi = 0.126$) and 775 nm ($\varphi = 0.026$) for RhoI, RhoBTA and RhoMQ, respectively (Fig. 1b and Table S1†). By contrast, RhoMA exhibited very weak fluorescence, which might be due to predominant vibration relaxation mediated energy dissipation (Fig. S2†). This result demonstrated that these chromophores exhibited large Stokes shifts. Moreover, the highly emissive properties suggested that these chromophores were in the zwitterionic "open" form with extended π-conjugation systems at physiological neutral pH.

We then investigated the spirocyclic "closed" and zwitterionic "open" properties of these chromophores in different pH solutions. RhoI exhibited a major absorption peak at 515 nm with a minor shoulder at 600 nm in acidic pH (Fig. S3†). The absorbance at 515 nm gradually decreased with concurrent increased absorbance at 600 nm as pH increased. Fluorescence measurements showed that RhoI was weakly fluorescent at acidic pH and the fluorescence intensity at 727 nm continuously increased with increasing pH. This result demonstrated that RhoI was predominantly in the spirocyclic "closed" form at acidic pH and "zwitterionic" form at physiological pH. The pK_{cycl} value (the pH at which half of the chromophores existed in the spirocyclic "closed" form) based on absorbance was determined to be 5.1. Furthermore, RhoBTA exhibited increased absorbance at 536 nm and enhanced fluorescence at 575 nm as pH increased from 2.0 to 9.0 (Fig. S4†). The pK_{cycl} value was calculated to be 5.0. Similarly, RhoMQ exhibited an absorption peak at 510 nm at pH 2.0 which was gradually decreased with a concurrent increase in

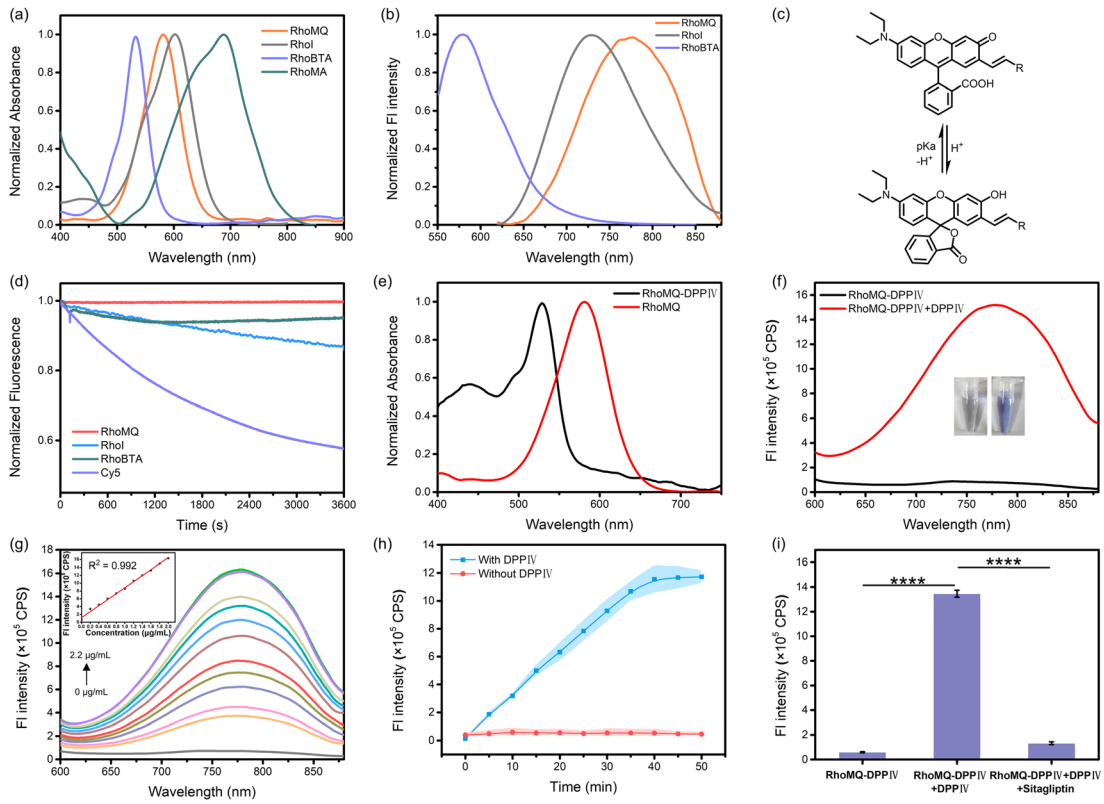

Fig. 1 (a) Normalized absorption spectra of RhoMQ, RhoI, RhoBTA and RhoMA (5 μM) in pH 7.4 buffer. (b) Normalized fluorescence spectra of RhoMQ, RhoI and RhoBTA (5 μM) in pH 7.4 buffer. (c) pH-dependent structural switching for xanthene-derived NIR chromophores. (d) Normalized fluorescence intensities for RhoMQ, RhoI, RhoBTA and Cy5 after irradiation for different times. (e) Normalized absorption spectra of RhoMQ-DPPIV and RhoMQ (5 μM) in pH 7.4 buffer. (f) Fluorescence spectra of RhoMQ-DPPIV (5 μM) with or without incubation with DPPIV (2.0 μg mL^{-1}) in pH 7.4 buffer. (Inset) Photographs of RhoMQ-DPPIV (left), RhoMQ-DPPIV and DPPIV (right). (g) Fluorescence responses of RhoMQ-DPPIV (5 μM) in the presence of varying concentrations of DPPIV (0–2.2 μg mL^{-1}) for 1 h. (Inset) Linear relationship between fluorescence intensities at 775 nm and the concentrations of DPPIV (0–2.0 μg mL^{-1}). (h) Time-dependent fluorescence intensities at 775 nm for RhoMQ-DPPIV (5 μM) with or without incubation with DPPIV ($n = 3$). (i) Fluorescence responses of RhoMQ-DPPIV (5 μM) toward DPPIV (2.0 μg mL^{-1}) without or with the inhibitor sitagliptin (50 μM) in pH 7.4 buffer. Statistical comparison was performed by a two-tailed t-test (****$p < 0.0001$, **$p < 0.01$, *$p < 0.05$, $n = 3$).

absorption at 580 nm as pH increased (Fig. S5†). The pK_{cycl} value was estimated to be 4.5. Concurrently, RhoMQ was essentially non-emissive at pH 2.0 which was gradually increased with increasing pH. Moreover, RhoMA exhibited an absorption peak at 500 nm at acidic pH which declined as pH increased (Fig. S6†). Meanwhile, there emerged a new absorption peak at 690 nm. The absorbance at 690 nm was increased by 140-fold as pH increased from 2.0 to 7.4. The pK_{cycl} value was determined to be 5.2. Collectively, these results demonstrated that the chromophores predominantly existed in the spirocyclic "closed" form at acidic pH and zwitterionic "open" form at physiological pH (Fig. 1c), suggesting their potential for developing high-contrast molecular probes for analyte detection and imaging in biological systems. It is worth noting that these chromophores obtained *via* extension of the conjugation system of xanthene at the 7 position exhibited pK_{cycl} values <5.2, suggesting that π-conjugation extension at the 7 position could be a general strategy to afford new chromophores with tunable NIR absorption and emission under physiological conditions. In addition, RhoBTA, RhoMQ and RhoI exhibited high photostability as compared to commercial fluorophore Cy5 (Fig. 1d). We chose RhoMQ and RhoMA for developing fluorescence and PA probes owing to their large Stokes shifts, high photostability and NIR emission or absorption wavelengths.

NIRF detection of DPPIV activity

The NIRF probe for DPPIV (RhoMQ-DPPIV) was first prepared by caging the phenolic hydroxyl group of RhoMQ with the DPPIV substrate Gly–Pro *via p*-aminobenzyl alcohol. RhoMQ-DPPIV exhibited a maximum absorption peak at 530 nm, which was blue-shifted by 50 nm compared to that for RhoMQ (Fig. 1e). Moreover, RhoMQ-DPPIV showed very weak fluorescence (Fig. S7†). These results indicated that RhoMQ-DPPIV existed in the spirocyclic form, which was ascribed to the caging of the phenolic hydroxyl group.

Next, we investigated the responsiveness of the RhoMQ-DPPIV probe to DPPIV. As anticipated, the fluorescence emission at 775 nm was dramatically increased upon incubation with 2.0 μg mL^{-1} DDPIV for 1 h (Fig. 1f). Concurrently, the absorbance at 530 nm was remarkably decreased and there emerged a strong absorption peak at 580 nm, which coincided with that for RhoMQ at neutral pH (Fig. S8†). This result suggested that RhoMQ-DPPIV was in the zwitterionic "open" form upon incubation with DPPIV, which was ascribed to DPPIV cleavage mediated release of RhoMQ. We employed ESI-MS and HPLC assays to verify the reaction mechanism. ESI-MS analysis showed there emerged a new peak with an *m*/*z* of 555.45 after reaction, which was ascribed to $[M]^+$ for RhoMQ (Fig. S9†). HPLC showed that RhoMQ-DPPIV was efficiently transformed to RhoMQ upon reaction with DPPIV (Fig. S10†). These results confirmed that RhoMQ-DPPIV was responsive to DDPIV.

We further tested the ability of RhoMQ-DPPIV to detect DPPIV activity. The fluorescence intensity at 775 nm gradually increased as the concentration of DPPIV increased from 0 to 2.2 μg mL^{-1} (Fig. 1g), and the fluorescence signal was enhanced by ~145-fold in the presence of 2.2 μg mL^{-1} DPPIV. Moreover, the fluorescence intensity was linearly correlated with the concentration of DPPIV in the range of 0 μg mL^{-1} to 2.0 μg mL^{-1}, and the limit of detection was calculated to be 2.3 ng mL^{-1}. Further time-dependent measurements showed that RhoMQ-DPPIV quickly responded to DPPIV within 5 min, and reached a maximum at 40 min (Fig. 1h). These results demonstrated that RhoMQ-DPPIV was capable of detecting DPPIV activity with high sensitivity and rapid kinetics. Selectivity studies showed that the fluorescence response of RhoMQ-DPPIV was highly selective to DPPIV with negligible increases in the presence of other common biological substances and several prolyl-cleaving peptidase enzymes (Fig. S11†). Moreover, the specific response of RhoMQ-DPPIV was verified by using sitagliptin, a specific DPPIV inhibitor.[25,28] The fluorescence was dramatically decreased for RhoMQ-DPPIV in the presence of DPPIV and sitagliptin (Fig. 1i). HepG2 cell lysate with positive expression of DPPIV also delivered intense fluorescence which was largely decreased in the presence of sitagliptin (Fig. S12†). These results demonstrated that RhoMQ-DPPIV was specifically activated by DPPIV. In addition, enzyme kinetic results showed that the Michaelis–Menten constant of RhoMQ-DPPIV to DPPIV was 12.37 μM (Fig. S13†), which was much smaller than in previous reports.[29,30] The values of K_{cat} and K_{cat}/K_m were determined to be 4.53 s^{-1} and 3.66 × 10^5 s^{-1} M^{-1}, respectively.

Fluorescence imaging of DPPIV activity in living cells

First, the cytotoxicity of RhoMQ-DPPIV was examined using a CCK-8 assay. HepG2 and HEK293T cells exhibited over 90% viability upon incubation with up to 100 μM RhoMQ-DPPIV, suggesting its good biocompatibility (Fig. S14†). Then, we explored the ability of RhoMQ-DPPIV to image DPPIV activity in live cells. Confocal laser scanning microscopy (CLSM) images showed that HepG2 cells incubated with RhoMQ-DPPIV displayed intense fluorescence (Fig. 2a and b). By contrast, the fluorescence signal was significantly reduced when HepG2 cells were pre-incubated with the DPPIV inhibitor sitagliptin. Flow cytometry showed a consistent result that HepG2 cells treated with RhoMQ-DPPIV showed strong fluorescence which was significantly decreased in the presence of sitagliptin (Fig. 2c).

DPPIV is an enzyme dysregulated in various pathological diseases especially tumors. We then explored the capability of RhoMQ-DPPIV to detect and image DPPIV activity in different cell lines. We found that RhoMQ-DPPIV treated HepG2, PC3 and MCF-7 cells delivered strong fluorescence signals (Fig. 2d and e). By contrast, there were very weak fluorescence signals from RhoMQ-DPPIV in A549, HeLa and HEK293T cells. This result implied DPPIV activity was high in HepG2, PC3 and MCF-7, but low in A549, HeLa and HEK293T cells, which was consistent with previous reports.[22,29] Furthermore western blotting confirmed that the different DPPIV activities were ascribed to the varying DPPIV expression levels (Fig. S15†). Moreover, flow cytometry assays showed the fluorescence signals of RhoMQ-DPPIV treated HepG2, PC3 and MCF-7 cells were dramatically decreased upon pretreatment with the inhibitor sitagliptin (Fig. 2f and S16†). These results demonstrated that RhoMQ-DPPIV was capable of detecting DPPIV activities in different cell lines.

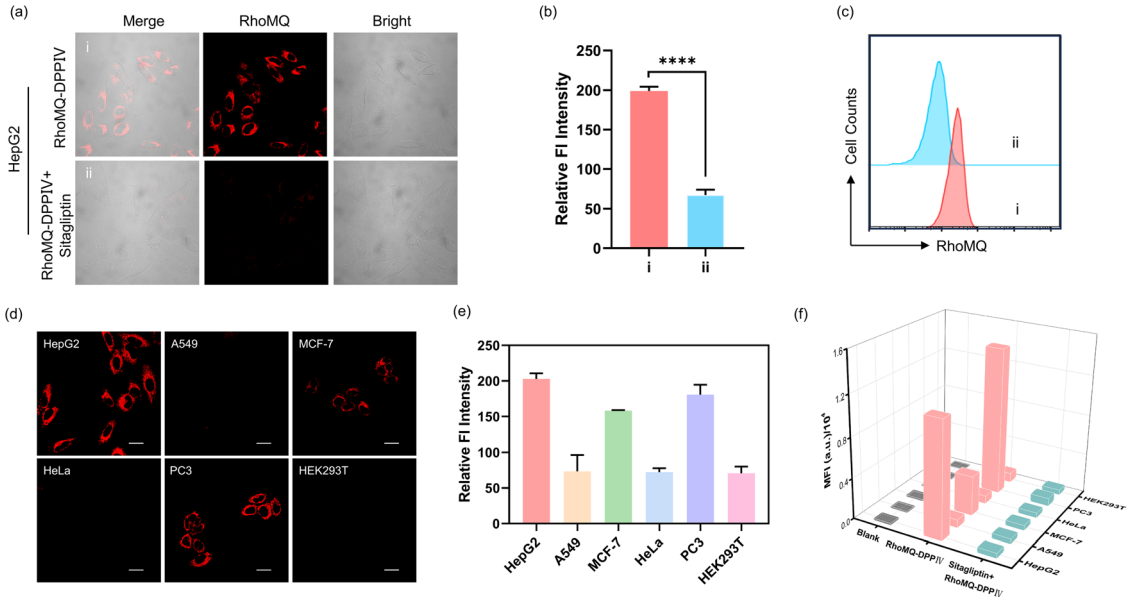

Fig. 2 Fluorescence imaging of DPPIV activity in living cells. CLSM images (a) and relative fluorescence intensity (b) for HepG2 cells incubated with RhoMQ-DPPIV (5 μM, 1 h) under different treatments: (i) HepG2 cells treated with RhoMQ-DPPIV (5 μM) for 1 h; (ii) HepG2 cells pre-treated with sitagliptin (50 μM, 1 h) and incubated with RhoMQ-DPPIV (5 μM, 1 h). (c) Flow cytometry analysis of HepG2 cells incubated with RhoMQ-DPPIV (5 μM, 1 h) without or with sitagliptin (50 μM). CLSM images (d) and relative fluorescence intensity (e) for various cell lines treated with RhoMQ-DPPIV (5 μM, 1 h). (f) Flow cytometry analysis for various cell lines treated with RhoMQ-DPPIV with or without sitagliptin. Scale bar = 25 μm. Data are presented as the mean ± s.d.

PA detection and imaging of DPPIV activity

We chose RhoMA to develop a PA probe for DPPIV owing to its NIR absorption in the zwitterionic form with a large blue shift in the spirocyclic form. A PA probe, RhoMA-DPPIV, for DPPIV was prepared by coupling RhoMA with the dipeptide substrate Gly–Pro *via* a self-immolative *p*-aminobenzyl alcohol. RhoMA-DPPIV showed a maximum absorption peak at 540 nm (Fig. 3a). The absorption peak was blue-shifted by 150 nm as compared to that for RhoMA in neutral pH, which coincided with that for RhoMA in acidic pH, suggesting that RhoMA-DPPIV was in the spirocyclic "closed" form. The responsiveness of RhoMA-DPPIV to DPPIV was then investigated using absorption and PA spectroscopy. The absorption peak for RhoMA-DPPIV was red-shifted to 690 nm after incubation with DPPIV for 60 min (Fig. S17†). Similarly, there was negligible PA signal in the range of 680–800 nm for RhoMA-DPPIV (Fig. 3b). By contrast, the PA signal at 690 nm was increased by 19-fold after incubation with 2.0 μg mL^{-1} DPPIV (Fig. 3c). Moreover, a specificity assay showed that the PA signal for RhoMA-DPPIV was sharply decreased in the presence of the inhibitor sitagliptin. This result suggested that RhoMA-DPPIV was in the zwitterionic "open" form after incubation with DPPIV. Further ESI-MS and HPLC analysis verified that RhoMA-DPPIV was converted to RhoMA after reaction with DPPIV (Fig. S18†). Together, this result demonstrated the capability of RhoMA-DPPIV for high-contrast PA detection of DPPIV.

We further explored the possibility of RhoMA-DPPIV for quantitatively detecting DPPIV activity *via* PA. The PA signals at 690 nm dynamically increased as the concentrations of DPPIV increased from 0 to 2.0 μg mL^{-1} (Fig. 3d). Further analysis revealed that the PA intensity was proportional to the concentration of DPPIV in the range of 0–2.0 μg mL^{-1} with a limit of detection of 2.5 ng mL^{-1}. Moreover, there were negligible PA signals at 690 nm for RhoMA-DPPIV incubated with several biologically relevant substances and several prolyl-cleaving peptidase enzymes (Fig. S19†). In addition, time-dependent measurements showed that RhoMA-DPPIV responded quickly to DPPIV within 5 min and reached a maximum at ~40 min (Fig. S20†). These results showed that RhoMA-DPPIV was capable of detecting DPPIV activity with high sensitivity, rapid kinetics and high specificity.

We then explored the probe to image DPPIV activity *via* PA in living cells. The cytotoxicity of RhoMA-DPPIV was first evaluated. The cell viability for HepG2 and HEK293T cells treated with RhoMA-DPPIV (0–100 μM) was over 90%, indicating that RhoMA-DPPIV was highly biocompatible (Fig. S21†). Multi-spectral optoacoustic tomography (MSOT) imaging showed that HepG2 cells with overexpression of DPPIV delivered intense PA signals with increasing RhoMA-DPPIV concentration (Fig. 3e and f). Moreover, the PA amplitude was remarkably decreased for HepG2 cells treated with sitagliptin. This result showed that RhoMA-DPPIV was capable of PA imaging of DPPIV activity in live cells.

NIRF/PA imaging of DPPIV activity *in vivo*

Motivated by the excellent performance of RhoMQ-DPPIV and RhoMA-DPPIV *in vitro* and in live cells, we then investigated the possibility of these two probes to image DPPIV activity *via* NIRF and PA *in vivo*. First, we explored the ability of RhoMQ-DPPIV and RhoMA-DPPIV to image DPPIV activity through chicken breast tissue. As expected, there was a weak NIRF signal for DPPIV activated RhoMQ-DPPIV embedded in 1 mm tissue,

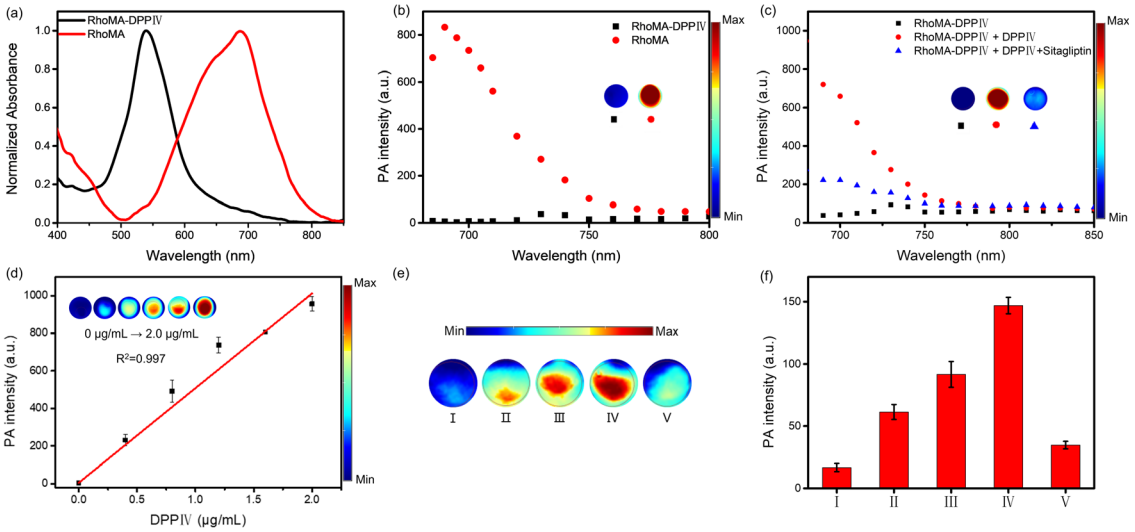

Fig. 3 PA responses of RhoMA-DPPIV toward DPPIV activity. (a) Absorption spectra for RhoMA-DPPIV (5 μM) and RhoMA (5 μM) in pH 7.4 buffer. (b) PA spectra and imaging of RhoMA-DPPIV (5 μM) and RhoMA (5 μM) in pH 7.4 buffer. (c) PA spectra and imaging of RhoMA-DPPIV (5 μM) in the presence of DPPIV (2.0 μg mL^{-1}) without or with sitagliptin (50 μM) at 37 °C in pH 7.4 buffer. (d) Linear relationship and PA imaging between PA intensities at 690 nm and various concentrations of DPPIV (0–2.0 μg mL^{-1}). MSOT imaging (e) and relative PA intensity (f) of HepG2 cells incubated with different concentrations of RhoMA-DPPIV (0–5 μM) under different treatments: (I) HepG2 cells treated without RhoMA-DPPIV for 1 h; (II) HepG2 cells treated with RhoMA-DPPIV (1 μM) for 1 h; (III) HepG2 cells treated with RhoMA-DPPIV (2 μM) for 1 h; (IV) HepG2 cells treated with RhoMA-DPPIV (5 μM) for 1 h; (V) HepG2 cells pre-treated with sitagliptin (50 μM, 1 h) and treated with RhoMA-DPPIV (5 μM) for 1 h. Data are presented as the mean ± s.d.

whereas RhoMA-DPPIV treated with DPPIV still displayed evident PA signals through up to 1 cm tissue (Fig. S22†). Then, HepG2 cells were implanted into the left flanks of the BALB/c nude mice to establish the tumour-bearing mouse model. We first tested the ability of the fluorescent probe RhoMQ-DPPIV to image DPPIV activity *via* tail-vein injection (Fig. 4a). The tumour-bearing mice were randomly divided into three groups (n = 3) and injected with PBS, RhoMQ-DPPIV, inhibitor sitagliptin and RhoMQ-DPPIV, respectively. Fluorescence imaging was then acquired at different time points. The mice injected with RhoMQ-DPPIV showed an evident NIRF signal at the tumour site at 2 h post-injection (Fig. 4b). The NIRF signal reached a maximum at 3 h and then gradually decreased until 12 h post-injection. By contrast, there were no appreciable fluorescence signals at the tumour site for control mice treated with PBS at each time point. The average NIRF signal at tumour sites in mice was enhanced by 3.8-fold at 3 h post-injection as compared to the control group treated with PBS (Fig. 4c). This result indicated that RhoMQ-DPPIV was activated at the tumour sites. To verify its specific activation by DPPIV, we pre-injected the tumour-bearing mice with the inhibitor sitagliptin. As anticipated, the NIRF intensity at the tumour sites substantially decreased as compared to the tumour-bearing mice treated with RhoMQ-DPPIV only at each acquisition time point (Fig. 4b and c). In addition, ex vivo NIRF imaging of dissected organs at 3 h post-injection showed intense NIR fluorescence in the liver and kidneys, which was presumably because the probe was mainly metabolized and cleared by these two organs (Fig. 4d and S23†). The RhoMQ-DPPIV fluorescence showed good colocalization with the immunofluorescence from DPPIV, suggesting that RhoMQ-DPPIV was selectively activated by DPPIV (Fig. S24†). These results demonstrated that RhoMQ-DPPIV was specifically activated by DPPIV in the tumour sites and could be employed for detecting DPPIV activity *in vivo*.

Subsequently, we explored the potential of PA probe RhoMA-DPPIV for imaging DPPIV activity *in vivo*. Similarly, HepG2 tumour-bearing mice were randomly divided into three groups (n = 3) and injected with PBS, RhoMA-DPPIV, and the inhibitor sitagliptin and RhoMA-DPPIV, respectively. MSOT images showed that the PA signal at the tumour sites began to appear at 2 h post-injection of RhoMA-DPPIV, and reached a maximum at ~3 h, followed by a gradual decrease until 12 h (Fig. 4e). By contrast, the mice treated with PBS showed negligible PA signal at 690 nm throughout the acquisition period. The PA signal at the tumour site was increased by approximately 6.8-fold at 3 h post-injection of RhoMA-DPPIV as referenced to the control mice treated with PBS (Fig. 4f). Similarly, the PA amplitude was remarkably decreased for mice pre-treated with the inhibitor sitagliptin. Similar to RhoMQ-DPPIV, mice injected with RhoMA-DPPIV also displayed strong PA signals in the liver and kidneys at 3 h post-injection (Fig. S25†). These results indicated that RhoMA-DPPIV was specifically activated by DPPIV activity in the tumour sites, allowing high-contrast imaging of DPPIV activity *in vivo*. To our knowledge, this is the first PA probe that enabled PA imaging of DPPIV activity *in vivo*. In addition, hematoxylin–eosin (H&E) analysis of major organs including the heart, liver, spleen, lungs and kidneys for mice treated with RhoMQ-DPPIV or RhoMA-DPPIV showed no abnormal cell morphology and tissue lesions (Fig. S26†). Additional blood chemistry analysis revealed that RhoMQ-DPPIV and RhoMQ-DPPIV exhibited negligible effect on the hepatic–renal function (Fig. S27†). These results imply their low toxicity and good biocompatibility. Together,

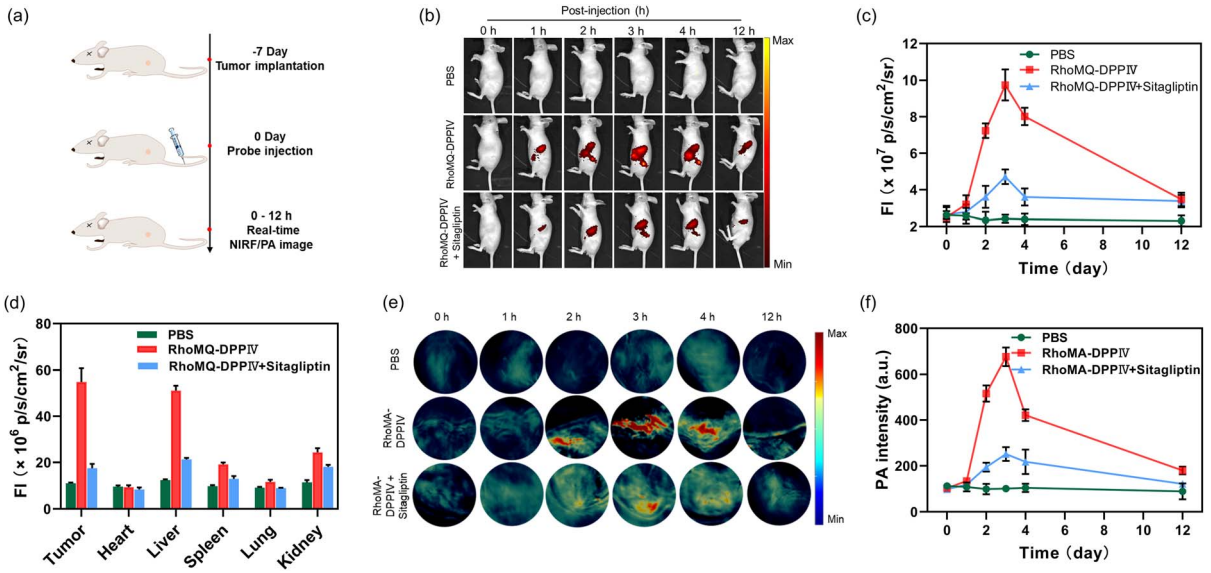

Fig. 4 *In vivo* NIRF/PA imaging of DPPIV activity in HepG2 tumor-bearing mice. (a) Schematic illustration of NIRF/PA imaging of DPPIV activity *in vivo*. (b) Representative NIRF imaging of HepG2 tumor-bearing mice upon tail-vein injection of RhoMQ-DPPIV (100 μM, 100 μL) with or without sitagliptin (100 μM) at different time points, with PBS as a control. (c) Time-dependent fluorescence intensities of HepG2 tumor-bearing mice at different time points under different treatments ($n = 3$). (d) Fluorescence intensities of dissected major organs and tumor tissues from the mice at 3 h post injection. (e) Representative PA imaging of HepG2 tumor-bearing mice upon tail-vein injection of RhoMA-DPPIV (100 μM, 100 μL) with or without sitagliptin (100 μM) at different time points, with PBS as a control. (f) Time-dependent PA intensities of HepG2 tumor-bearing mice at different time points under different treatments ($n = 3$). Data are presented as the mean ± s.d.

these results demonstrated that RhoMQ-DPPIV and RhoMA-DPPIV were capable of detecting DPPIV activity *via* NIRF/PA imaging with high specificity *in vivo*.

Conclusions

In conclusion, we developed a class of new chromophores by extending the conjugation system of a xanthene scaffold with different electron withdrawing groups at the 7 position. It was shown that these new chromophores exhibited red-shifted absorption and emission wavelengths, large Stokes shifts and high photostability. It was demonstrated that these chromophores exhibited a pH-tunable equilibrium between a spirocyclic "closed" and a zwitterionic "open" form. We further develop two activatable probes by caging the phenolic hydroxyl groups of RhoMQ and RhoMA with the DPPIV substrate. It was demonstrated that these two probes allowed NIR fluorescence and PA detection and imaging of DPPIV activity with high sensitivity, high specificity and rapid kinetics *in vitro* and in live cells. Moreover, these probes allowed high-contrast NIR fluorescence and PA imaging of DPPIV activity in a tumour bearing mouse model *in vivo*. This result highlights the promise of π-conjugation expansion of xanthene chromophores at position 7 for developing high-contrast molecular probes.

Data availability

Main experimental data are provided within the main text and the ESI.† Additional data are available from the corresponding author upon reasonable request.

Author contributions

F. Wang and J. H. Jiang conceived the project and wrote the manuscript. W. Dong edited the manuscript. P. Lu synthesized the compounds and collected experimental data. S. Dai and H. Zhou participated in *in vitro* characterization assays. All authors discussed the results and commented on the manuscript.

Conflicts of interest

There are no conflicts to declare.

Acknowledgements

This work was supported by the National Key Research Program (2019YFA0905800, 2018YFA0902301), National Natural Science Foundation of China (22274040, 22322404, 22374041), Science and Technology Major Project of Hunan Province (2021SK1020), and Hunan Provincial Science Fund for Distinguished Young Scholars (2022JJ10004).

Notes and references

1 Z. Cheng, E. J. Thompson, L. Mendive-Tapia, J. I. Scott, S. Benson, T. Kitamura, A. Senan-Salinas, Y. Samarakoon, E. W. Roberts, M. A. Arias, J. Pardo, E. M. Galvez and M. Vendrell, *Angew. Chem., Int. Ed.*, 2023, **62**, e202216142.
2 S. He, J. Li, Y. Lyu, J. Huang and K. Pu, *J. Am. Chem. Soc.*, 2020, **142**, 7075–7082.

3 J. I. Scott, Q. Deng and M. Vendrell, *ACS Chem. Biol.*, 2021, **16**, 1304–1317.
4 Z. Zeng, S. S. Liew, X. Wei and K. Pu, *Angew. Chem., Int. Ed.*, 2021, **60**, 26454–26475.
5 A. L. Antaris, H. Chen, K. Cheng, Y. Sun, G. Hong, C. Qu, S. Diao, Z. Deng, X. Hu, B. Zhang, X. Zhang, O. K. Yaghi, Z. R. Alamparambil, X. Hong, Z. Cheng and H. Dai, *Nat. Mater.*, 2016, **15**, 235–242.
6 C. Wang, W. Du, C. Wu, S. Dan, M. Sun, T. Zhang, B. Wang, Y. Yuan and G. Liang, *Angew. Chem., Int. Ed.*, 2021, **61**, e202114766.
7 L. V. Wang and S. Hu, *Science*, 2012, **335**, 1458–1462.
8 Q. Li, S. Li, S. He, W. Chen, P. Cheng, Y. Zhang, Q. Miao and K. Pu, *Angew. Chem., Int. Ed.*, 2020, **59**, 7018–7023.
9 J. Huang and K. Pu, *Angew. Chem., Int. Ed.*, 2020, **59**, 11717–11731.
10 Z. Wang, T. C. Detomasi and C. J. Chang, *Chem. Sci.*, 2021, **12**, 1720–1729.
11 D. Englert, E.-M. Burger, F. Grün, M. S. Verma, J. Lackner, M. Lampe, B. Bühler, J. Schokolowski, G. U. Nienhaus, A. Jäschke and M. Sunbul, *Nat. Commun.*, 2023, **14**, 3879.
12 Y.-L. Huang, A. S. Walker and E. W. Miller, *J. Am. Chem. Soc.*, 2015, **137**, 10767–10776.
13 Y. M. Poronik, K. V. Vygranenko, D. Gryko and D. T. Gryko, *Chem. Soc. Rev.*, 2019, **48**, 5242–5265.
14 N. Li, T. Wang, N. Wang, M. Fan and X. Cui, *Angew. Chem., Int. Ed.*, 2023, **62**, e202217326.
15 P. Wang, L. Yu, J. Gong, J. Xiong, S. Zi, H. Xie, F. Zhang, Z. Mao, Z. Liu and J. S. Kim, *Angew. Chem., Int. Ed.*, 2022, **61**, e202206894.
16 T.-B. Ren, W. Xu, W. Zhang, X.-X. Zhang, Z.-Y. Wang, Z. Xiang, L. Yuan and X.-B. Zhang, *J. Am. Chem. Soc.*, 2018, **140**, 7716–7722.
17 S. Zeng, X. Liu, Y. S. Kafuti, H. Kim, J. Wang, X. Peng, H. Li and J. Yoon, *Chem. Soc. Rev.*, 2023, **52**, 5607–5651.
18 G. Jiang, X. F. Lou, S. Zuo, X. Liu, T. B. Ren, L. Wang, X. B. Zhang and L. Yuan, *Angew. Chem., Int. Ed.*, 2023, **62**, e202218613.
19 C. S. L. Rathnamalala, S. Hernandez, M. Y. Lucero, C. B. Swartchick, A. Kalam Shaik, N. I. Hammer, A. K. East, S. R. Gwaltney, J. Chan and C. N. Scott, *Angew. Chem., Int. Ed.*, 2023, **62**, e202214855.
20 D. Liu, Z. He, Y. Zhao, Y. Yang, W. Shi, X. Li and H. Ma, *J. Am. Chem. Soc.*, 2021, **143**, 17136–17143.
21 L. L. Baggio, E. M. Varin, J. A. Koehler, X. Cao, Y. Lokhnygina, S. R. Stevens, R. R. Holman and D. J. Drucker, *Nat. Commun.*, 2020, **11**, 3766.
22 K. Ohnuma, R. Hatano and C. Morimoto, *Nat. Immunol.*, 2015, **16**, 791–792.
23 J. Z. Long and B. F. Cravatt, *Chem. Rev.*, 2011, **111**, 6022–6063.
24 H. B. Rasmussen, S. Branner, F. C. Wiberg and N. Wagtmann, *Nat. Struct. Biol.*, 2003, **10**, 19–25.
25 C. Hollande, J. Boussier, J. Ziai, T. Nozawa, V. Bondet, W. Phung, B. Lu, D. Duffy, V. Paradis, V. Mallet, G. Eberl, W. Sandoval, J. M. Schartner, S. Pol, R. Barreira da Silva and M. L. Albert, *Nat. Immunol.*, 2019, **20**, 257–264.
26 D. S. Ghorpade, L. Ozcan, Z. Zheng, S. M. Nicoloro, Y. Shen, E. Chen, M. Bluher, M. P. Czech and I. Tabas, *Nature*, 2018, **555**, 673–677.
27 K. N. Wang, L. Y. Liu, D. Mao, S. Xu, C. P. Tan, Q. Cao, Z. W. Mao and B. Liu, *Angew. Chem., Int. Ed.*, 2021, **60**, 15095–15100.
28 K. Wang, Z. Zhang, J. Hang, J. Liu, F. Guo, Y. Ding, M. Li, Q. Nie, J. Lin, Y. Zhuo, L. Sun, X. Luo, Q. Zhong, C. Ye, C. Yun, Y. Zhang, J. Wang, R. Bao, Y. Pang, G. Wang, F. J. Gonzalez, X. Lei, J. Qiao and C. Jiang, *Science*, 2023, **381**, eadd5787.
29 J. Valverde-Pozo, J. M. Paredes, T. J. Widmann, C. Griñan-Lison, G. Ceccarelli, A. Gioiello, M. E. Garcia-Rubiño, J. A. Marchal, J. M. Alvarez-Pez and E. M. Talavera, *ACS Sens.*, 2023, **8**, 1064–1075.
30 L. W. Zou, P. Wang, X. K. Qian, L. Feng, Y. Yu, D. D. Wang, Q. Jin, J. Hou, Z. H. Liu, G. B. Ge and L. Yang, *Biosens. Bioelectron.*, 2017, **90**, 283–289.